Acta Materialia 242 (2023) 118437

Contents lists available at ScienceDirect

Acta Materialia

journal homepage: www.elsevier.com/locate/actamat

Full length article

Strong silicon oxide inclusions in iron

Alejandra Slagter[a,*], Joris Everaerts[a,b], Léa Deillon[a,c], Andreas Mortensen[a]

[a] Mechanical Metallurgy Laboratory, École Polytechnique Fédérale de Lausanne, MXD 140 (Bâtiment MXD), Station 12, Lausanne CH-1015, Switzerland
[b] Department of Materials Engineering, KU Leuven, Kasteelpark Arenberg 44 box 2450, Leuven 3001, Belgium
[c] Department of Mechanical and Process Engineering, ETH Zürich, Technoparkstr. 1, Zürich 8005, Switzerland

ARTICLE INFO

Article history:
Received 10 June 2022
Revised 13 September 2022
Accepted 13 October 2022
Available online 14 October 2022

Keywords:
Micromechanics
Oxide inclusions

ABSTRACT

Oxide inclusions are ubiquitous in steel and are known to affect, generally in a negative sense, the mechanical performance of steel products. Micromechanical properties of those phases are therefore important, yet they have remained largely unexplored. We present strength measurements performed on individual silicon oxide inclusions in iron. The inclusions are produced in laboratory-fabricated samples by silicon deoxidation of high-purity iron melts containing dissolved oxygen. Spherical silica inclusions of diameter ~3 μm thus produced are notched using ion milling and then tested in bending for their strength, by loading under displacement control *in-situ* within a scanning electron microscope. Results show that silicon oxide inclusions thus precipitated within iron are amorphous in structure, exhibit a smooth outer surface, and have fracture strains in the range from 8 to 17%, corresponding to fracture stress levels on the order of 10 GPa. The strength of silicon oxide inclusions precipitated in iron can hence approach the highest values so far measured in dry silica. The presence within iron and its alloys of precipitated silica thus need not be deleterious, and might perhaps even be exploited to produce novel high-strength materials.

1. Introduction

Non-metallic inclusions are small discrete second phases that appear in the microstructure of metal alloys as a result of the fabrication processes, and which are generally known to degrade alloy mechanical properties [1]. Oxide inclusions appear in steel primarily for two reasons: (i) co-precipitation of oxygen dissolved within the metal, and (ii) the entrainment, by flowing steel, of slag, refractory, or surface oxide. The latter mechanisms produce "exogenous" inclusions, which are generally large in size and hence the most dangerous. Exogenous inclusions are nowadays largely suppressed thanks to modern clean liquid metal treating, handling, and casting practices. Precipitated or "indigenous" inclusions, on the other hand, are in steel an unavoidable consequence of the relatively high solubility of oxygen in liquid iron, which decreases during alloy cooldown and solidification, and as a result, produces either gas or the precipitation of oxides within the metal. In order to avoid outgassing during casting operations (also called effervescence), which in steels is linked to the formation of carbon oxides during solidification, deoxidizer elements (such as Al, Si or Mn) are added to the melt; those act as a trap for the dissolved oxygen by forming either liquid or solid oxide precipitates within the molten steel. Although many of the indigenous inclusions are subsequently eliminated by flotation, an important fraction remains in the liquid steel and becomes part of the alloy microstructure. As once pointed out by Kiessling [1], one ton of steel with an oxygen content as low as 1 ppm will contain between 10^6 and 10^{11} inclusions if those are present as spherical Al_2O_3 inclusions with a diameter between 100 and 1 micrometers.

Oxide inclusions are important because they influence the mechanical properties of steel: they affect ductility and toughness [2] and they can be responsible for the initiation of cracks leading to fatigue failure [3,4]. It has been shown that the melting practice, including factors such as the type of slag used, the lining of the refractories, or the melting atmosphere, can have a large influence on characteristics of the produced inclusions, and through this on steel properties; the most salient example of this being given by the fatigue resistance of bearing steels [5]. In order to improve steel quality, "inclusion engineering" techniques [6] have been developed that go beyond controlling the size and number of non-metallic inclusions (NMI), to also enable modifications of their shape and, to some extent, of their nature by means of thermochemical treatment based on analysis coupled with extensive databases.

* Corresponding author.
E-mail address: alejandra.slagter@epfl.ch (A. Slagter).

https://doi.org/10.1016/j.actamat.2022.118437

In contrast with the vast amount of thermochemical data relevant to inclusions in steel, the literature dedicated to their structure and mechanical properties is quite limited. Probably the most comprehensive reference work was compiled in 1978 by Kiessling and Lange [7], who gathered, in an atlas-like book, optical microscopy images and the chemical composition of inclusions observed in steels of the time. In addition, they fabricated synthetic oxide mixtures that reproduced the observed compositions in sufficiently large volumes to enable phase analysis using X-ray diffraction and Vickers's hardness measurements, using techniques that at the time did not have the spatial resolution required to characterize individual inclusions.

Such has been the advancement of techniques available for the measurement of local material properties that it is now possible to study the structure and mechanical behavior of individual phases having volumes as small as a few cubic micrometers. To date only a few studies have made use of these novel tools to characterize steel inclusions. Among those are the contributions of Lamagnere et al. [8], Stiénon et al. [9], and Wang et al. [10], who used nanoindentation to probe the hardness and elastic modulus of different types of non-metallic inclusions, and more recently the work of Kusche et al. [11] who performed micropillar compression experiments on manganese sulphide inclusions. Although few in number, these studies show that much can be learned about the mechanical behavior of these small precipitates, unique not only because of their size and shape but also because of their chemistry and structure, which are determined by the complex chemical equilibria and thermo-mechanical history of the steel within which they are contained.

We show here that micromechanical experiments can be carried out *in-situ* on individual oxide inclusions to measure their strength. The test methodology is an adaptation of the procedure presented in [12] and implemented in [13,14]; it consists in testing a pre-notched particle having the shape of a "C", by applying a compressive force normal to the notch. Milling of the notch is performed with a focused ion beam (FIB) and the experiments are coupled with finite element simulations to deduce the maximum tensile strain and stress at the point of fracture. An important advantage of this testing technique is that tensile stresses and fracture are developed in a region of the particle that has not been altered by FIB milling. We present here the results of such measurements carried out on silica inclusions that were precipitated within molten iron.

2. Materials and methods

2.1. Fabrication of iron samples containing oxide inclusions

SiO_2 inclusions were produced by Si-deoxidation of a high-purity iron melt containing oxygen. The main steps of the sample fabrication process involve: (i) induction melting of high purity iron lumps (99.98%, ABCR GmbH, Karlsruhe, Germany) containing a few ppm of oxygen in a cold crucible furnace under a 99.998% pure argon atmosphere to 1600±50 °C, (ii) the addition of a controlled amount of Si by dropping a Fe-5 wt% Si pre-alloy (produced with an arc-melter) into the melt; and (iii) cool-down and solidification of the sample.

High purity iron is selected as the base material, as opposed to a specific steel composition, in order to control, to the best possible extent, the composition of the oxide inclusions that precipitate. The same reason justifies the use of a cold crucible setup instead of a more conventional ceramic crucible, since it was observed that contact of high-purity molten iron with a ceramic crucible leads to the incorporation of elements from the crucible into the inclusions.

The cold crucible set-up used to prepare samples, shown in Fig. 1, has as its main element a copper crucible that is continuously cooled with water, in which the charge is melted by induction heating. The crucible is placed inside a sealed quartz tube which allows to control the atmosphere by evacuating air to a pressure of 10^{-2} mbar, purging 4 times, and filling with argon of 99.998% purity. Temperature is measured by means of a two-color pyrometer (Impac ISR 6 Advanced, LumaSense Technologies, Milpitas, CA).

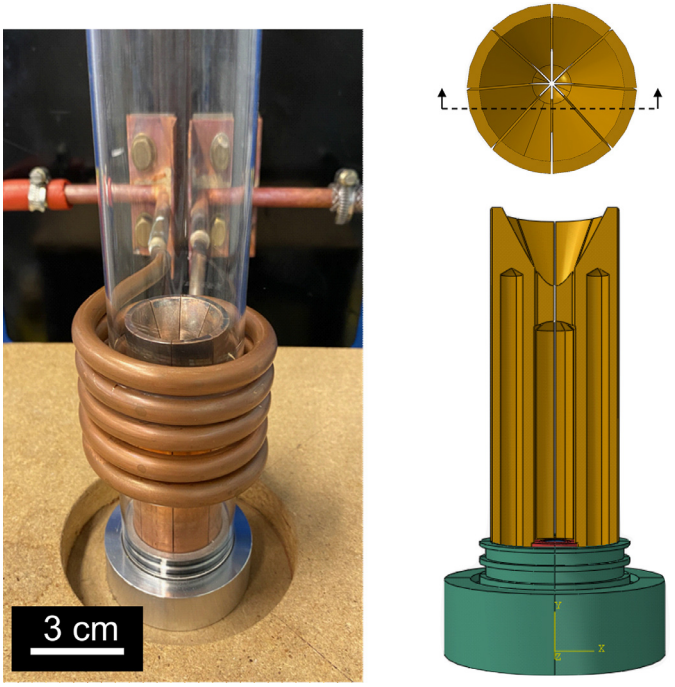

Fig. 1. Photograph and cross-section schematic of the cold crucible set-up used for the fabrication of inclusion-containing iron samples.

The iron lumps used for sample production are of high purity, yet were not produced by vacuum remelting; as a consequence they contain residual amounts of oxygen. The oxygen content in the lumps was measured by the inert gas fusion technique (LECO ON 736, LECO, St. Joseph, MI) and was found to be on the order of 200–300 ppm. The precipitation of oxide inclusions in samples of this work is thus the result of the reaction between these ppm of oxygen present in the liquid iron and the silicon that was added to the melt.

2.2. Characterization techniques

The oxide inclusions were characterized by standard metallography along cut and polished cross-sections of the iron samples. Scanning Electron Microscopy (SEM) imaging was performed at 3 kV using a Zeiss Gemini SEM 300 (Oberkochen, Germany). The elemental composition of the inclusions was analyzed using Energy Dispersive Spectroscopy (EDS) (Oxford Instruments, Abingdon, UK) with an accelerating voltage of 8 kV. Selective dissolution of the iron matrix was conducted to partially expose oxide inclusions lying along the polished surface. This was done by electropolishing for 60 s the matrix in a dilute acidic solution (Struers A2 electrolyte, consisting of ~5% $HClO_4$ dissolved in a mixture of ethanol and 2-butoxyethanol). Inclusions exposed in this way were then machined into micromechanical test samples. Exposed inclusions were also analyzed for their structure using confocal Raman spectroscopy (inVia^{TM} confocal Raman microscope, Renishaw); spectra were collected with a 532 nm laser, using a x 100 objective and a confocal set up.

Fig. 2. Schematics of (a) the positioning of samples for FIB milling; (b) the notch geometry used for the testing of spherical inclusions (viewed along the direction of the ion or electron beams); (c) subsequent positioning of the sample for *in-situ* testing in the SEM.

Nanoindentation hardness measurements were performed using a Hysitron TI 950 (Bruker, Billerica, Massachusetts, US) and a Berkovich diamond tip on individual inclusions along the surface of polished samples. Accurate positioning of the indentations on the inclusions was possible thanks to the 500 nm resolution of the XY positioning platform of the instrument. A total of 15 indents were performed using a maximum load between 1 and 2 mN.

2.3. Micromechanical testing

Micromechanical test samples were carved out of partially exposed oxide inclusions by milling a deep notch with a Ga^+ Focused Ion Beam (FIB) (Zeiss CrossBeam 540, 30 keV, 20 pA to 300 nA). Spherical inclusions were specifically targeted for the fabrication of micromechanical test samples, not only because they correspond to the most commonly observed morphology in our samples, but also because their compact and simple geometry simplifies milling operations, modeling of the test, and interpretation of results. During the milling operation, the iron sample was mounted with its polished surface tilted to a 10° angle with respect to the Ga^+ beam axis (Fig. 2a), as this provides ion beam access to all inclusions that have been exposed along the surface of the sample. A V-shape geometry with a large root curvature radius (Fig. 2b) was used for the notch, instead of the rectangular profile adopted in previous work, to adapt the notch to the spherical shape of the silica inclusions. In addition, for most of the test samples, a portion of the upper lip of the "C" was removed to avoid closure of the C before fracture of the sample (Fig. 2b).

Testing of the C-shaped particles was performed *in-situ* within the SEM under a pressure of $\sim 10^{-6}$ mbar using a nanomechanical testing system (FemtoTools FT-NMT04, Buchs, Switzerland) equipped with rotation and tilt stages. A diamond flat punch, of diameter 5 µm or 10 µm, was used to impose a vertical displacement on the upper lip of the particles. The punch was mounted on a microelectromechanical sensing probe able to measure both normal and lateral forces up to ± 20,000 µN. Tests were performed at a constant displacement speed of 0.02 µm/s, leading to a strain rate along the outer surface of the particles in the range from 1 to 4×10^{-3} s^{-1}. The samples were aligned in such a way that the direction of the ion beam used in the milling step was (i) parallel to the observation direction during testing and (ii) perpendicular to the diamond punch displacement direction (Fig. 2c). Measurements were performed while observing the test in the SEM, with the exception of four additional tests that were performed with the electron beam off, so as to test whether data were affected by exposure to the electron beam. SEM operating parameters during micromechanical tests were a voltage of 3 keV on a FEG source, with a current below 200 pA scanning an area on the order of 60 μm^2 over the $\sim$ 180 s duration of the test. The cleanliness of the flat punch tip surface was confirmed regularly by SEM inspection and the tip was cleaned when necessary following the procedure detailed in Ref. [15].

The system compliance, including the elastic deformation of the iron matrix and that of the frame, was measured in separate experiments. These were performed in the vicinity of tested particles by collecting force-displacement data while compressing, one at a time, the top of partly exposed spherical inclusions that had not been FIB-milled.

The total load point displacement measured while compressing emerging intact spherical inclusions is the sum of displacements caused by the elastic deformation of the load train, by compression of the iron matrix under the particle, and by deformation of the (unnotched) particles under the punch. Knowing that loads during C-shaped particle testing are too small to cause plastic deformation in the iron matrix, the contribution to system compliance of compression of the iron matrix under the particle can be estimated using Sneddon's equation; this returns values, for all tested particles, below 2.17 10^{-3} µm/mN, well below measured load train compliance values (on the order of 0.1 µm/mN, see below). This particle-size dependent contribution to the compliance can, thus, be neglected. The other particle-size dependent part of the signal is associated with (intact) spherical particle deformation in the punch/particle contact region. The punch displacement (δ) associated with particle deformation under the indenter can be estimated using Hertz contact theory formulated for a hard punch against a spherical elastic solid [16] (Eq. (1)):

$$\delta = \left[\frac{9P^2\left(1-\nu_p^2\right)^2}{16\ E_p^2 R} \right]^{\frac{1}{3}} \tag{1}$$

where P is the load acting on the particle of radius R (measured from SEM images), E_p and ν_p are elastic constants for isotropic silica (Young's modulus and Poisson's ratio, respectively, taken to equal E_p =72 GPa and ν_p =0.17 [17,18]). Calculated values of δ were then subtracted from the force-displacement data of each intact sphere test, to compute the (constant) system compliance that accounts for contributions coming only from the load train including the punch and the iron substrate. This compliance was found to be relatively constant from one particle to the other and during each intact particle compression test (thus validating the approach), and to be on the order of 0.11 µm/mN (equivalent to a stiffness of 9000 N/m).

No signs of plastic deformation were observed in the iron during the micromechanical tests; permanent deformation of the iron matrix was only observed during compliance measurement tests performed on small particles at relatively high loads that were above the load range used when testing inclusions in the same size range.

2.4. Finite element simulations

Finite-element models of each test were formulated using Abaqus/CAE 6.14–1 (Dassault Systèmes Simulia Corp., Providence, RI, USA, 2014) in order to compute the local strain and stress within the inclusion at the moment of fracture, or at peak load if

Table 1
Abaqus/CAE FEM cap-plasticity parameter values, defined first in the word terminology of the Abaqus Documentation, then between parentheses using word and variable terminology from Ref. [20].

Model/Parameter		**Model A** - as reported in [19,20]	**Model B** (modification of Model A to delay tensile yield)
Material Cohesion (yield strength in pure shear, d) (GPa)		7.5	11.5
Angle of Friction (friction angle, β)		0.001	0.001
Cap Eccentricity (R)		1.53	1
Initial Yield Surface Position (initial volumetric strain, $\varepsilon_{pl}^{vol}\|_o$)		0	0
Transition Surface Radius (yield surface parameter, α)		1	1
Flow Stress Ratio (yield surface anisotropy in the deviatoric plane, K)		1	1
Cap hardening parameters	p_{c0}	11.5	11.5
	p_c (at 1% strain)*	12.5	12.5

* Equivalent to a hardening slope (ξ) of 100 GPa.

the notched particle did not fail before the notch was completely closed. The 10° tilt of the iron surface was not accounted for in computations, such that calculations were conducted on three-dimensional models comprising half of each tested, partially embedded, notched silica particle. Meshes were built using quadratic tetrahedral elements (C3D10), with the geometry and dimensions of the particles as measured from SEM images. The particles were assumed to be isotropic, with the same elastic constants as above ($E_p = 72$ GPa and $\nu_p = 0.17$ [17,18]).

In addition to models assuming linear elastic deformation of the silica phase, a second FEM model was run for each fractured particle, in which it was assumed that silica also experiences plastic deformation as dictated by the yield criterion proposed by Kermouche et al. [19]. This was implemented in Abaqus/CAE through the Abaqus Cap Plasticity model using parameters from Ref. [20] and is listed in Table 1 as Model A. This yield criterion considers that plasticity in silica can be caused not only by shear loading, where the yield stress is characterized by a pure shear critical stress (d in the terminology of Ref. [20]), but also by pure hydrostatic compression, where the onset of plastic densification is characterized by a critical pure hydrostatic compressive yield stress (p_c in the terminology of Ref. [20]). Values for (compressive) yielding according to parameters of Ref. [20] correspond to $d = 7.5$ GPa and $p_c = 11.5$ GPa. In this model, plastic deformation driven by hydrostatic pressure is only present in compression, while for stress states comprising hydrostatic tension, yield is only driven by shear following a classical Von Mises criterion.

Finally, a third, modified elastoplastic, FEM model was run for each fractured particle, using a similar yield criterion but modified to raise d to 11.5 GPa. This was implemented in order to delay yield in tensile stress space and, through this, to confine plastic deformation to the inner notch radius, where the stress state is compressive (see Discussion).

Given the large deformations attained during the micromechanical tests, geometric nonlinearity was included in the models, meaning that the dimensional change of elements that accompanies their deformation was accounted for in subsequent calculations of both stress and strain. The punch was simulated as a discrete rigid element (i.e., as a flat shell) to which the experimentally measured, compliance-corrected, displacement was imposed. Contact between punch and particle was modeled using classical isotropic Coulomb friction with a penalty friction formulation. The friction coefficient in each model was considered constant and equal to the average ratio of lateral to normal forces registered by the force sensor during the corresponding test, with the observed friction coefficient situated between 0.05 and 0.3. In order to reproduce experimental conditions, in which sliding between the punch and particle surfaces was evidenced, the maximum shear stress allowed at the contact area was set to a low value, namely 600 MPa.

Boundary conditions for the lower end of the half-particle were set as a restriction of displacements in all directions (pinning) of an area along the particle bottom surface, with that area defined by the intersection of the particle surface with a plane perpendicular to the loading direction (Fig. 3). This (rigid) boundary condition creates a site of stress concentration along the particle surface, situated just above the line of intersection of the (rigid) matrix surface with the particle surface. This poses no problem if this site of stress concentration is remote from the peak stress region created by the notch along the outer particle surface while it is tested. Such was not the case in all tests, however; when this occurred (Figs. 3b&d illustrate this) the iron surface was lowered in FEM simulations to the highest position for which a minimum appears between the stress at the intersection of the particle surface with the iron surface and the peak stress along the particle opposite to the notch (Figs. 3c&e illustrate this).

3. Results

Most of the oxide inclusions produced in this work were smooth and spherical (Fig. 4a) and had diameters ranging between 1 and 5 μm. A comparatively smaller number of the oxide precipitates were observed to have a dendritic morphology (Fig. 4b) similar to that documented in Refs. [21,22], or alternatively a rosette morphology (Fig. 4c) analogous to that described in Ref. [23]. The elemental composition of oxides in present samples that were analyzed by EDS corresponds well with that of SiO_2. Nanoindentation measurements conducted on the silica inclusions give indications of permanent deformation under the indenter and return apparent values for the hardness of 9.0 ± 0.8 GPa and 79 ± 10 GPa for the apparent reduced modulus (average ± 2 times the standard deviation, here and in what follows). Those are apparent values, because the determination of both quantities is affected by the presence of the (stiffer) iron matrix surrounding the particle. Correcting for this effect using the scheme proposed in Ref. [24] returns 8.8 ± 0.8 GPa for the hardness and 74 ± 10 GPa for the Young's modulus, consistent with known values for amorphous silica (9.25 GPa and 72 GPa, respectively). No internal microstructural features or defects were found along cross sections through the inclusions.

Although thermodynamic considerations indicate that cristobalite is the stable form of silica at the temperature at which these oxides are likely to have precipitated (≈1600 °C), an amorphous structure for the present spherical oxide inclusions was confirmed by confocal Raman spectroscopy, Fig. 5. As seen, the inclusions give broad intensity shifts instead of narrow bands characteristic of crystalline structures; furthermore, intensity profiles resemble closely the spectrum measured for fused quartz while differing markedly from the spectrum emitted by crystalline quartz; see Fig. 1 of Ref. [25].

C-shaped particle bend tests led to significant deformation followed by sudden fracture of the inclusions in roughly one-third of the tests. Fracture surfaces of the broken inclusions were often irregular, showing signs of multiple crack formation. Some inclusions

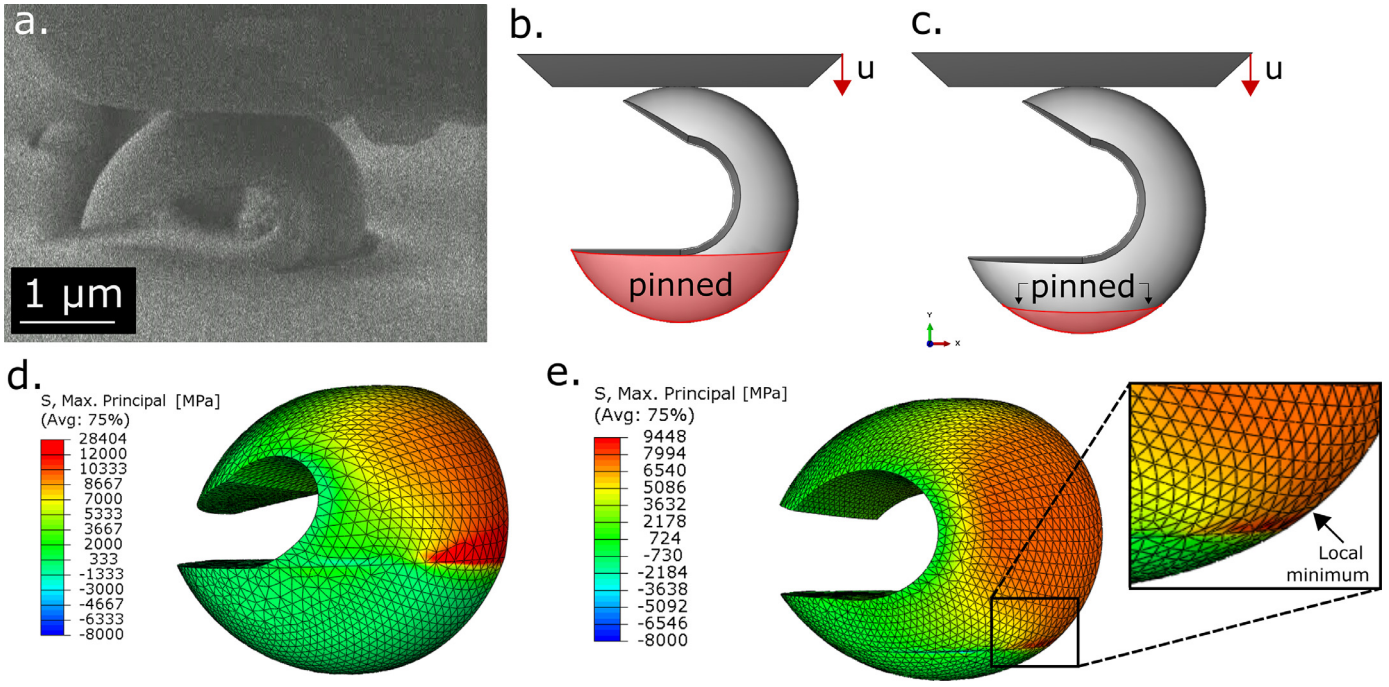

Fig. 3. Boundary conditions used in FEM model and results from simulations of mechanical tests: (a) SEM image of a tested inclusion at the moment of maximum displacement; (b) pinned area used in simulation, with zero surface displacement everywhere below the iron surface observed in (a); (c) same with pinned area top boundary lowered to prevent the development of a region of maximum principal stress along the limit of the pinned area; (d) maximum principal stress distribution predicted for the fully elastic model with the pinned area as defined in (b); (e) same but with pinned area as defined in (c).

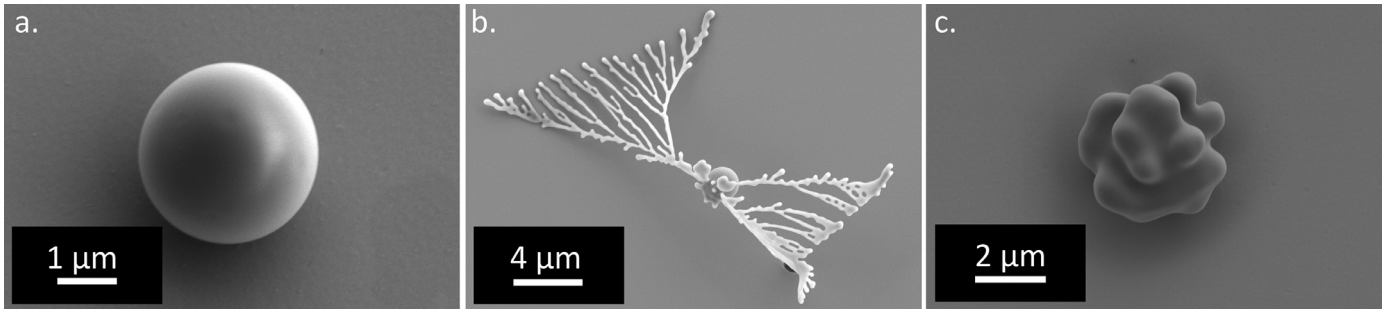

Fig. 4. SEM images of SiO_2 inclusions observed in iron alloy samples from laboratory deoxidation experiments. (a) spherical morphology; (b) dendritic morphology; (c) rosette morphology.

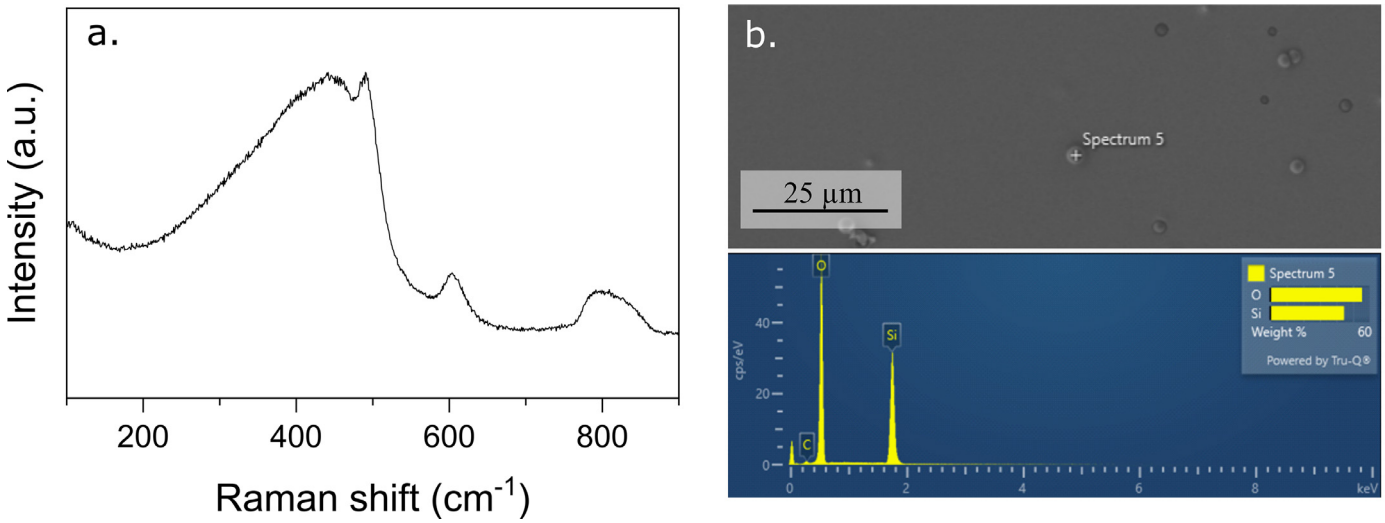

Fig. 5. (a) Raman spectrum, and (b) EDS spectrum, collected from SiO_2 inclusions observed in iron alloy samples from laboratory deoxidation experiments. Spectrum collected on inclusions exposed after dissolution of the iron matrix (by electropolishing).

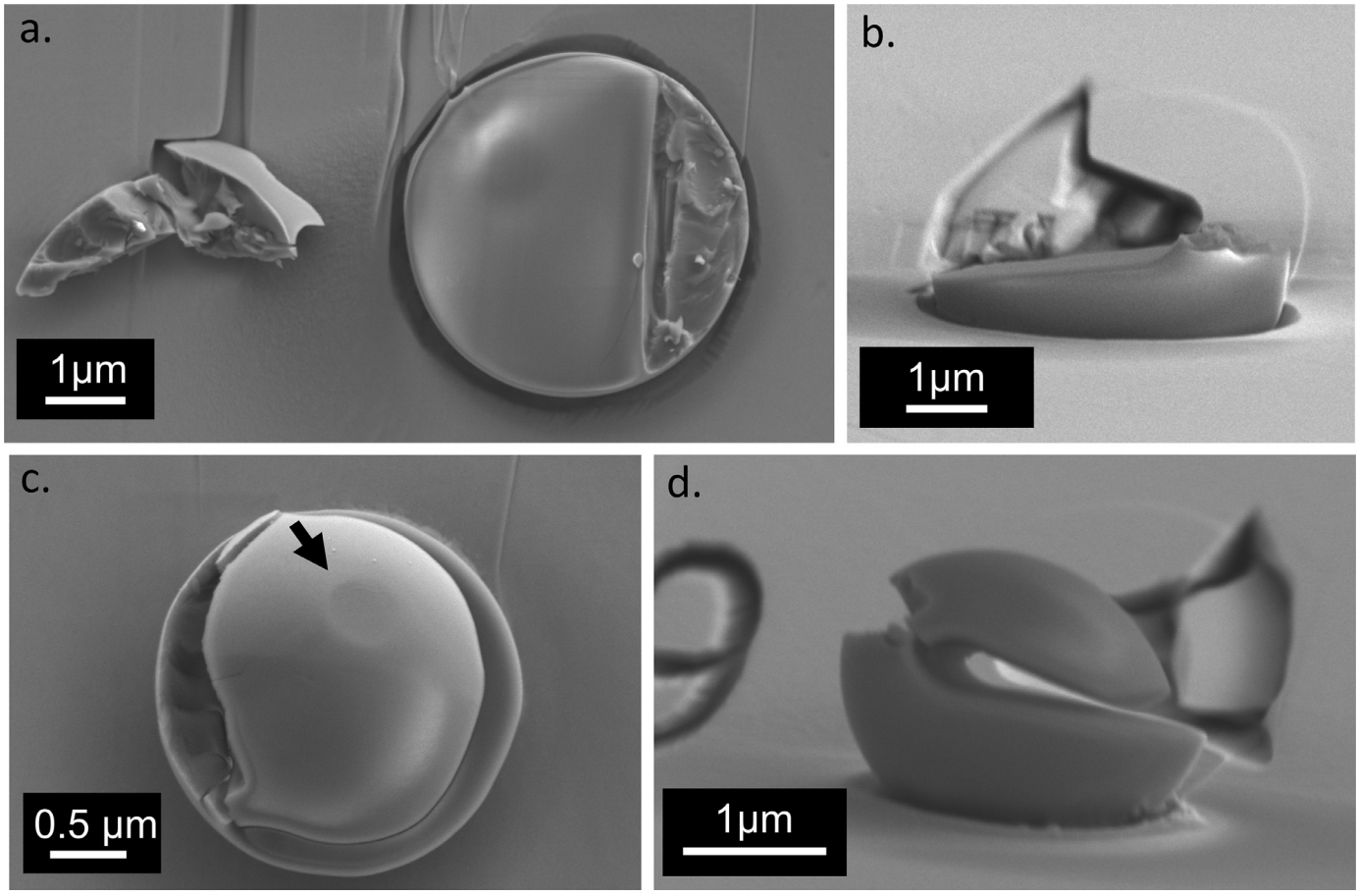

Fig. 6. Top, (a) and (c), and side, (b) and (d), view of two fractured particles after testing; note in (c) and (d) that the top portion of the particle remained roughly in place after fracture, and that one can discern (black arrow) a trace of the indenter along the top particle surface, betraying the presence of a small level of compressive silica plastic deformation.

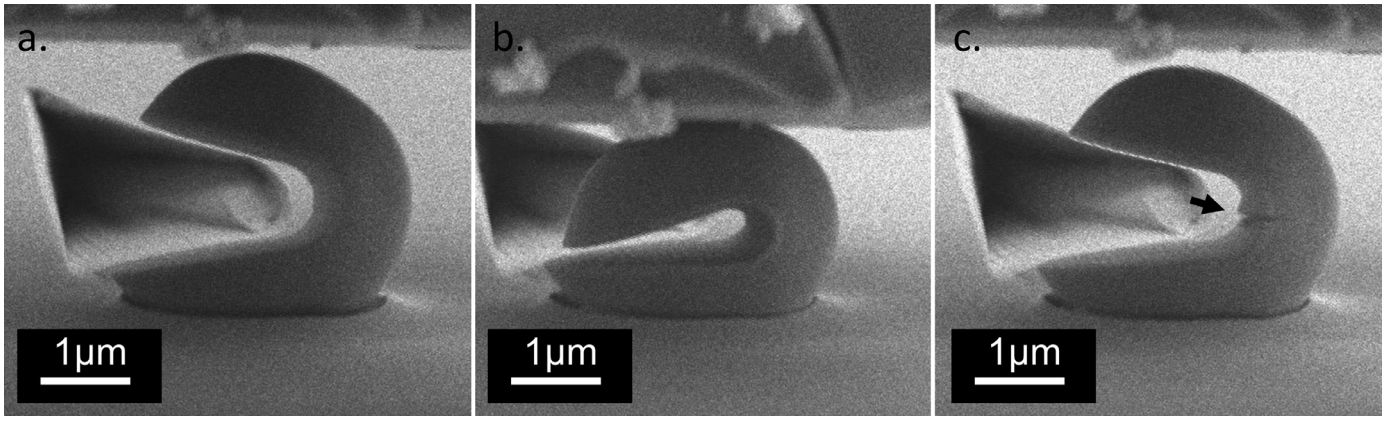

Fig. 7. Example of non-fractured particle (a) before testing, (b) at the moment of maximum displacement, (c) after unloading where a crack is visible in the inner part of the notch (black arrow).

were smashed by the indenter, while in others (the majority) the upper inclusion half landed at a location remote from the inclusion. Fig. 6 shows two inclusions for which the fracture surface was comparatively well preserved: in (a) and (b) an inclusion for which a relatively simple and clean fracture surface is seen, in (c) and (d) the single inclusion for which the upper part remained attached to the lower half of the inclusion. For the remaining samples (roughly two thirds) closure of the "C" was reached before fracture of the particle (Fig. 7), at which point the tests were stopped and the sample was rapidly unloaded. For some of the non-fractured particles (six out of twenty-seven), the opening of a small crack was observed along the inner, FIB-milled, surface of the notch during unloading; an example of this is given in Fig. 7c and indicated with a black arrow. Load-unload tests conducted while gradually bending C-shaped inclusions showed, even at small loads (below 100 μN), unloading load-displacement lines lower than the loading curve, thus indicating the presence of irreversible deformation in the C-shaped inclusion.

Force-displacement data (Fig. 8) show overall good agreement between experiments and FEM models. The initial portion of the

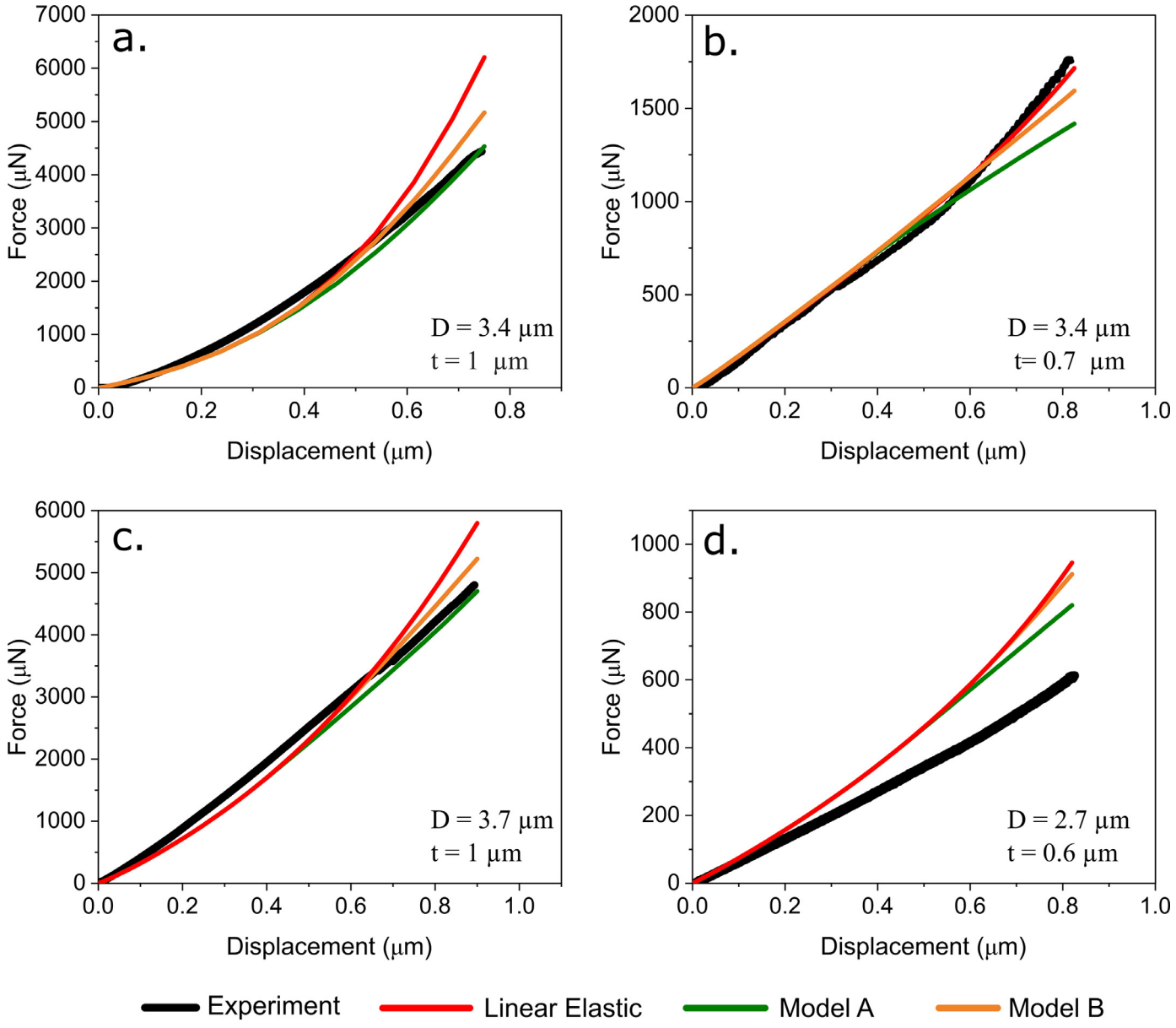

Fig. 8. Examples of force-displacement data collected from experiments and finite element simulations for four different tests along with each particle diameter (D) and ligament thickness (t); experimental data were corrected to account for the compliance of the substrate and the testing rig. Colours distinguish the curves in the on-line version; experimental data are plotted with a thicker line; simulation curves are ranked vertically downwards in the following order: linear elastic (top), Model B (middle), Model A (lowest).

curve is, as expected, not altered by the incorporation of plasticity in the models. Also as one would expect, at larger strain levels the force computed for both elasto-plastic models falls below values for purely linear elastic deformation; however, deviations remain small, both between different model predictions and between predictions and experimental data. The main trend observed is that the level of agreement between predictions and data decreases as the particle size decreases (Fig. 8d illustrates this). The sensitivity of simulations to dimensional input parameters, namely the ligament radius and thickness, as well as the angle of tilt of the compression axis with respect to the normal to the notch plane, was examined with a series of separate simulations. These are detailed in the Supplementary Material; those calculations show that the predicted load-displacement curve is highly sensitive to those geometrical parameters while the predicted peak stress and strain values are comparatively little affected by those variations.

Detailed model predictions show that (i) high stresses are present in the inner region of the notch, as a combination of shear and hydrostatic stress, and that (ii) the maximum principal stress is tensile and is always located at the outer surface of the C-shaped particles (Fig. 9), as one would expect. The incorporation of plastic behavior in the silica deformation law, using parameters proposed in Refs. [19,20] (Model A), leads to predict the presence of permanent deformation along both the inner and outer surfaces of the particle (Fig. 9c). This caps, as one would expect, the observed maximum principal stress at the assumed yield stress, of ~8 GPa, while slightly increasing the strain that simulations predict along the outer surface. Simulations carried out with a yield criterion modified to restrict plastification to the inner notch surface (Model B) show similar peak stress and strain facture values along the particle outer surface as those obtained assuming fully linear elastic deformation.

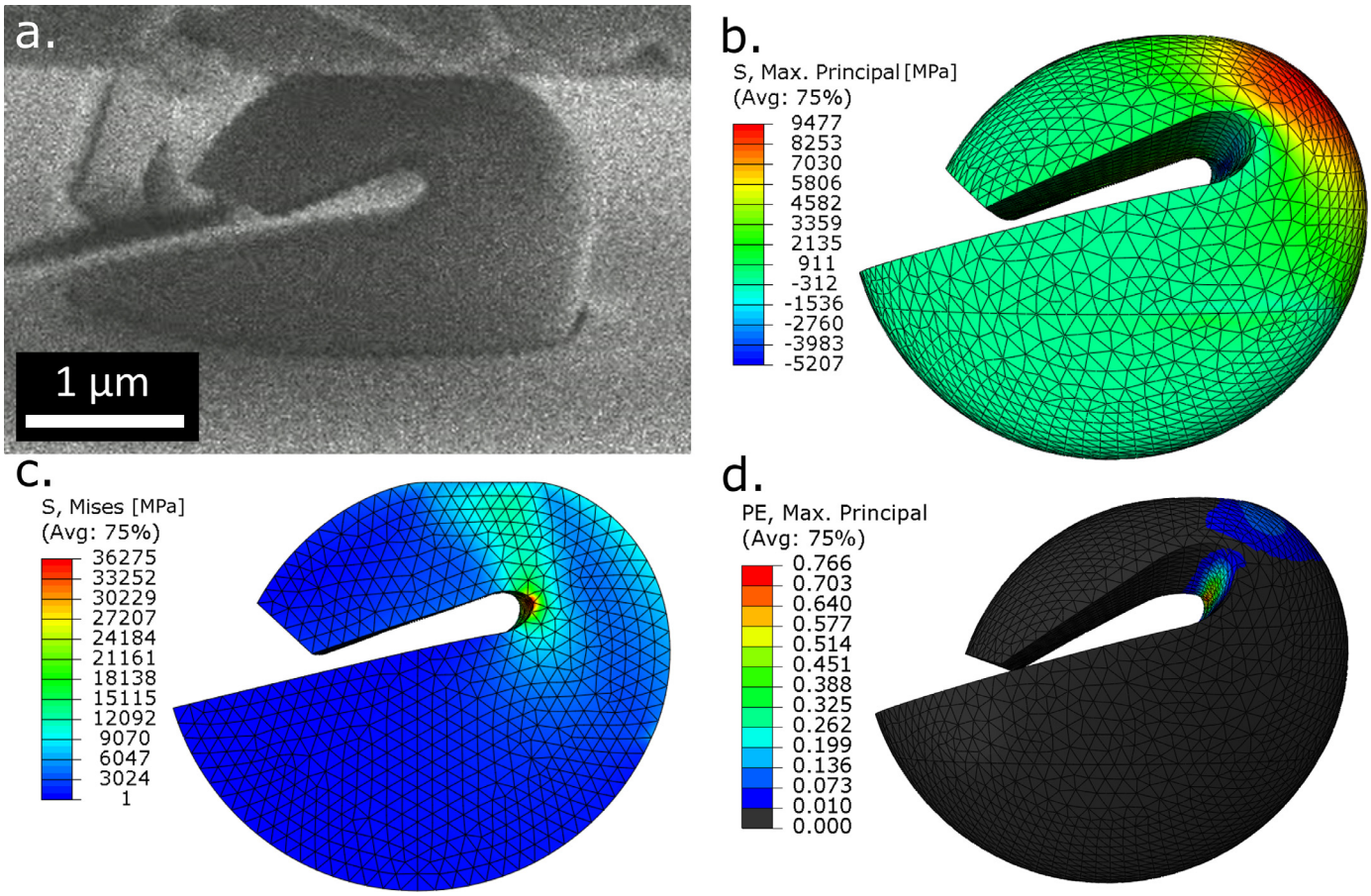

Fig. 9. SEM image of a particle at maximum imaged displacement before fracture (a) and FEM simulation results of: (b) maximum principal stress and (c) von Mises stress (along the mid-plane cross section of the particle), both assuming linear elastic behavior, and d) maximum principal plastic strain predicted for the particle modeled as an elasto-plastic solid with a deformation law defined by Model A.

Fig. 10a and 10c present values of the maximum principal strain and stress reached according to FEM models using a linear elastic deformation law, for particles that fractured (filled symbols) and particles that did not fail (open symbols), with an indication of data collected with the electron beam of the SEM turned off. Fig. 10b and 10d show the maximum strain and stress reached by fractured particles according to elasto-plastic models A and B (described in Section 2.3). Points are separated along the horizontal direction in the plots of this figure according to the product of the ligament thickness times the notch diameter times the particle diameter. This is a rough indicator of the stressed volume, since that volume scales roughly with each of those three lengths along each of three perpendicular directions.

4. Discussion

References in the literature to amorphous silica inclusions nucleated and grown within iron or its alloys are scarce. Early suggestions of the precipitation of glassy SiO_2 in iron can be found in the work of Forward [23] and Flemings [26]. A more recent mention to the amorphous structure of SiO_2 inclusions in iron and its alloys can be found in a review by Zhang and Thomas [27]. Gleining et al. [28] have argued that phases with the SiO_2 composition found in multiphase inclusions within 18CrNiMo7–6 case hardening steel were probably amorphous, since no diffraction lines from those phases were observed in Electron Back Scattered Diffraction (EBSD) experiments. Looking beyond steel, Wasai and Mukai [29] showed that amorphous silica can precipitate in silicon deoxidation experiments conducted with molten copper. The present data thus provide new, explicit, confirmation of the fact that amorphous SiO_2 forms within pure, oxygen-containing, iron in the presence of dissolved silicon. As a consequence, we believe that it would be relevant to adapt thermodynamic calculations involving SiO_2 formation in iron and its alloys to consider the amorphous form of silica as a possible deoxidation product, in addition to cristobalite. This can be important because, even if the structure of the Si-deoxidation product has a small impact on the total Gibbs free energy of the system, it could potentially have a large impact on the composition of the predicted phases since crystalline forms of SiO_2 have a limited solubility for other elements while the amorphous structure can incorporate relatively large amounts of other metals/metal oxides [30].

The second main observation emerging from the present data is the spectacularly high resistance to fracture that is measured here, by means of the C-shaped specimen bend test, in spherical amorphous silica inclusions. This result is unaffected by the electron beam, Fig. 10(a), since data with the beam off fall near the middle of the range displayed by *in-situ* data. This lack of a discernable influence of the relatively low-intensity beam of the SEM (compared to that of a TEM) on micromechanical measurements conducted on silica agrees with observations reported in Refs. [31,32].

Both elastic and elastoplastic simulations of deformation within the bent inclusions lead to conclude that, along their outer surface, tensile strains in the range from 8 to 17% were reached before inclusion fracture. Those are remarkably high levels of tensile strain for amorphous silica. Fracture strain values of this magnitude in glass are typical of high-perfection silica fibers fractured in two-point bend tests, which return fracture strain values in the range from 6 to 8.5% under ambient conditions (with 50% relative humidity), or from to 16 to 18% when testing is conducted under

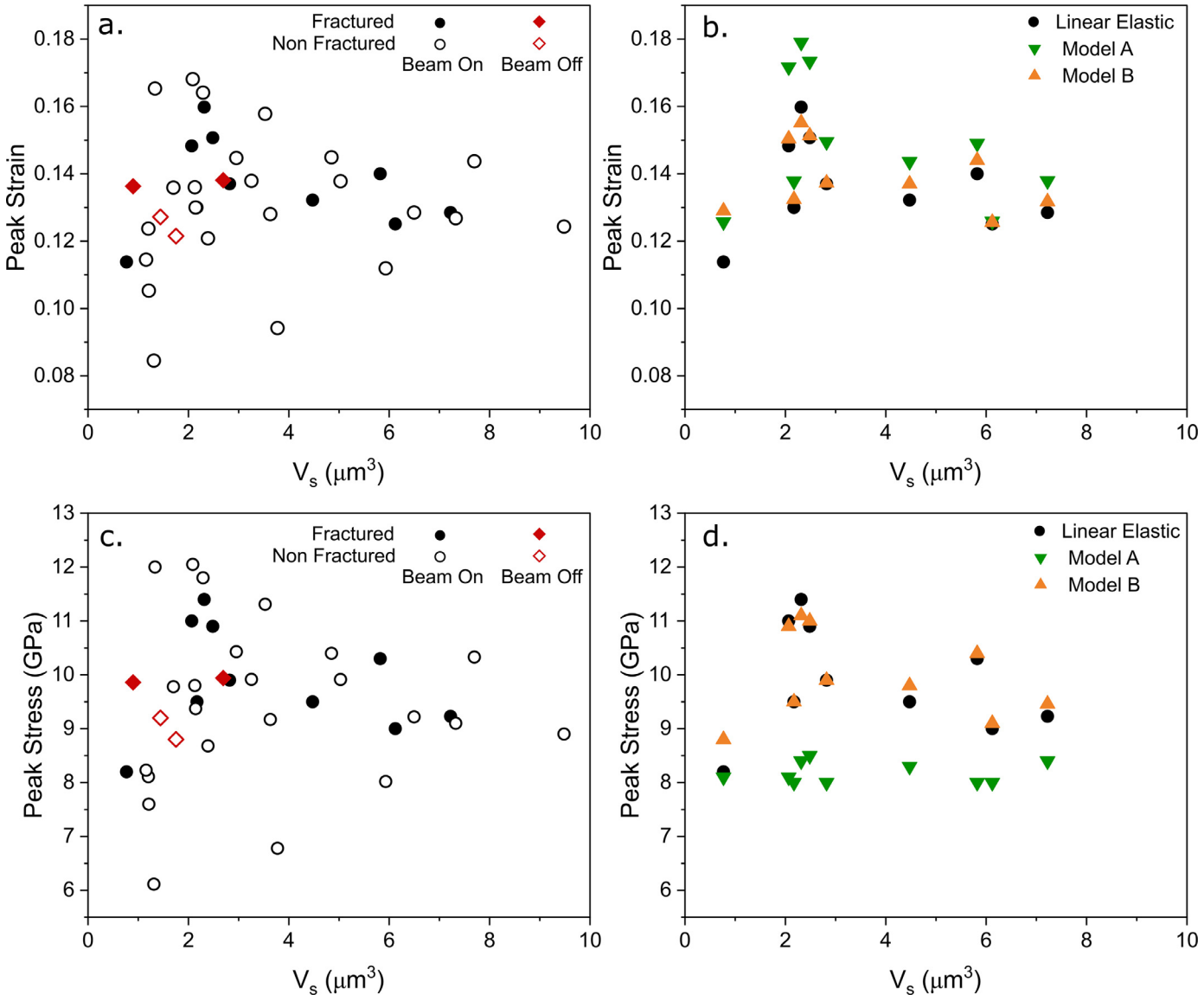

Fig. 10. Maximum principal strain and stress obtained by FEM modeling of the tests: (a) and (c) of all tested particles and assuming linear elasticity; (b) and (d) of particles that fractured, assuming linear elasticity or assuming elastoplastic behavior according to Models A or B (see Table 1). V_s is the product of the ligament thickness times the notch diameter times the particle diameter of each sample.

liquid nitrogen (i.e., free of the influence of moisture) [17,33–35]. In tensile testing, failure strain values in the same range (12–15%) are reported for metallized fibers that were coated from the melt [36]. Those values all exceed one-half of the intrinsic tensile fracture strain, situated near 20% [35,37,38], that was derived for silica tested under load-control knowing its strain-dependent modulus.

What is the corresponding failure stress? If one assumes fully linear elastic deformation, then the tensile strength values measured here for silica inclusions along their surface are predicted by finite element simulations to be on the order of 10 GPa, Fig. 10. This is again on the order of values measured in tensile testing for pure, high-quality silica fibers in either vacuum [39] or liquid nitrogen, where maximum reported values reach 14 GPa [17,38–41]. Values in the same range (12–15 GPa) are reported for metallized fibers that were coated from the melt [36]. Values measured with uncoated high-quality silica fibers in air, namely ~5–7 GPa [17,33,34,36,39,41,42], are noticeably lower, likely due to the effect of moisture in the testing environment.

For the large strain and stress levels observed in the current study, the implications of assuming a linear elastic behavior must, however, be considered, even if predictions from FEM simulations match relatively well recorded load-displacement curves (Fig. 8), since (i) the elastic modulus of silicate glasses is known to depend on strain, especially for high strain levels, and since (ii) significant plastic deformation has been observed in glass at high stress values.

It is known that the elastic modulus of amorphous silica increases by up to 25% upon uniaxial tensile straining, and does so at least up to strains on the order of 5 to 10% [37,38]. Measurements at higher strain levels are difficult, but extrapolations from lower strain data [37] show that the linear elastic assumption, for tensile conditions up to strains on the order of ~20%, underestimates the observed failure stress. So the influence of non-linear elasticity will be to *increase* the tensile strength values derived from the present data assuming linear elastic glass deformation, by an amount lower than 20% (given that the present tests are in essence bend tests [43]).

Load-unload cycles conducted on C-shaped inclusions gave, as mentioned above, signs of the presence of irreversible deformation. Plasticity, if present, will impose a cap on the maximum strength

of the inclusion material if plastic deformation can be triggered under tension. There is substantial evidence showing that amorphous silica can deform plastically to total strains in the order of 20% in experiments where the stress state is predominantly compressive, such as in indentation [20,44–46], diamond anvil cell compression [47], or micropillar compression testing [32,48–50]. The common observation in those experiments is that amorphous silica undergoes permanent deformation under stresses around 7 to 9 GPa, with evidence for both densification and shear as the underlying mechanisms that cause plasticity. In experiments of this study, the crack opening observed in the inner part of the notch during the unloading of some of the non-fractured C-shaped tests, Fig. 7c, and also the slight particle surface deformation that one can see at the top of the fractured particle half in Fig. 6c, indicate (in the location marked with a black arrow) that some level of plastic deformation indeed occurred in regions of the inclusions that were subjected to compressive stress states of sufficiently high value (and, for the notch root region, to modification by gallium ion implantation). Linear elastic finite element simulations also suggest that plastification is to be expected in the inner region of the notch while the C-shaped inclusions were bent: predicted Von Mises stress values at that location, for at least some of the linear elastic model calculations (those with thicker ligaments), reach values near 35 GPa.

We therefore also conducted finite element simulations assuming the presence of plasticity in the amorphous silica inclusions. We used a model derived directly from the literature (Model A), and then modified it in a way to see, in simulations, silica plastification only in regions of the inclusions subjected to compressive stress states (Model B, produced by raising the shear yield stress in Model A). The reason for imposing this restriction is that there are no signs in our data, nor to the best of our knowledge in the literature [20], that plastic deformation appears in amorphous silica when it is deformed under predominantly tensile stress. In present samples the outer surface across the notch root in bent samples (see Fig. 7c) remains smooth after unloading, with no sign of permanent deformation or rippling that would likely result if the outer surface had experienced substantial plastic elongation while the inclusion was under maximum load, given that upon unloading that region would experience a compressive surface state. More generally, the failure of high-strength amorphous silica fibers in bending or tensile testing is regularly reported to be brittle, with flat fracture surfaces (when they can be observed) [51]. Furthermore, if amorphous silica were prone to deform plastically under tension, then its toughness should exceed twice its surface energy. It is thus most likely that plastic deformation was experienced only in the inner part of the C-shape and not on the outer surface of deformed C-shape inclusions, leading us to believe that strain and stress values experienced by inclusions tested here are probably better predicted by Model B than by Model A. Predictions of both models are plotted in Fig. 10(b) and (d) for samples that experienced fracture. Predictions of Model A for the tensile failure stress of fractured particles remain (obviously) capped by the assumed tensile yield stress. Predictions of Model B come close to values predicted by linear elasticity (in fact they exceed slightly predictions from linear elasticity for both strain and stress, which is a priori not expected; likely this is a result of densification on the compressive side of the notch). We thus conclude that compressive plastic deformation in the material does not affect significantly peak tensile fracture stress values that emerge from the present experiments.

It is unlikely that the etching step used to expose the inclusions would explain why such high failure strains were reached here, because (i) silica is non-conductive and hence was not electrolytically etched while the matrix was removed; (ii) exception made for hydrofluoric or phosphoric acid, which were not used here, amorphous high-purity silica is known to be inert in acidic environments [52], and finally (iii) where high-strength glass fibers have been etched in corrosive environments, their strength is nearly always found to have *decreased* [17,52–55] (an exception is with fibers that have a rough or damaged surface, the strength of which can be increased from lower values to a few GPa by means of an etch that reduces the depth of surface irregularities, however, this situation does not apply here [17]).

In summary, the very high strains to failure that are measured here are thus likely not affected by artefacts, leading us to conclude that silica inclusions precipitated within iron in the present work display, along their surface, tensile strength and strain values that match what has been reported for the strongest silica fibers produced to date, namely values in the range 8 - 17% for strain, and 6 – 11 GPa for stress. Those values come near the upper limit of what is known to be possible in amorphous silica; using a simple fracture mechanics back-of-the-envelope calculation, since for amorphous silica $K_{Ic} \approx 0.75$ MPa$\sqrt{\text{m}}$ [17], peak defect depths are therefore everywhere below 1 to 3 nm along the inclusion surfaces. Since in steel the amorphous silica phase is isolated from the surrounding atmosphere, it is also reasonable to expect the inclusions to be shielded from water and thus retain their high strength over prolonged periods of time, the sole (but important) exception being inclusions located along the surface of the metal.

In turn, assuming that the tested inclusion regions are representative of the entire inclusions, this implies first that it is possible to deoxidize iron without necessarily introducing weak defects in its midst if the inclusions can be made to be strongly bonded to the matrix. We have not tested here the strength of the particle/matrix interface (this is the subject of ongoing work); however, unless it is quite weak (in which case interfacial voiding might weaken steel containing such inclusions), and unless they emerge at the surface of the metal, the present inclusions are likely not to fracture within iron, even when the alloy is subjected to elevated tensile stress. A second implication of findings reported here is that, given its high fracture stress, perhaps amorphous silica precipitated within iron might be used as a reinforcing phase. If equally smooth and strong amorphous silica inclusions can be produced in much larger proportions within steel, then one would have made a material with an admittedly lowered modulus, but with a potentially high strength to density ratio, entirely made from abundant elements (iron, carbon, silicon and oxygen), and – if one can bypass initial silica reduction - with a potentially lower carbon footprint than steel given that only a portion of the material would be reduced from ore.

5. Conclusion

Silicon oxide inclusions can be formed by deoxidation of high-purity, oxygen-containing, iron melts with the addition of silicon-iron pre-alloys. The oxides formed in this way are frequently spherical with an amorphous structure and a smooth outer surface.

The fracture stress of spherical amorphous silica inclusions thus formed can be measured using an adaptation of the C-shaped microsample testing method that was developed to test, free of FIB artefacts, the strength of reinforcing phases within metallic materials. Results show that failure strains in the range from 8 to 17% are attained, corresponding to strength values of the silica inclusions that reach or exceed (since most particles tested reached such values without breaking) the range from 6 to 11 GPa. Those values approach the upper bound for the strength of dry amorphous silica: oxide inclusions in steel can be very strong.

Data availability

The raw and processed data from this work are available for download from the Zenodo website at https://zenodo.org/ under the following digital object identifier (DOI):10.5281/zenodo.6623275.

Declaration of Competing Interest

The authors declare that they have no known competing financial interests or personal relationships that could have appeared to influence the work reported in this paper.

Acknowledgments

This work was sponsored by the Swiss National Science Foundation, (Grant No. 200021_182557).

Supplementary materials

Supplementary material associated with this article can be found, in the online version, at doi:10.1016/j.actamat.2022.118437.

References

[1] R. Kiessling, Clean steel: a debatable concept, Met. Sci. 14 (5) (1980) 161–172.
[2] André Luiz Vasconcellos da Costa e Silva, The effects of non-metallic inclusions on properties relevant to the performance of steel in structural and mechanical applications, Journal of materials research and technology 8 (2) (2019) 2408–2422, doi:10.1016/j.jmrt.2019.01.009.
[3] S.X. Li, Effects of inclusions on very high cycle fatigue properties of high strength steels, Int. Mater. Rev. 57 (2012) 92–114, doi:10.1179/1743280411Y.0000000008.
[4] U. Zerbst, M. Madia, C. Klinger, D. Bettge, Y. Murakami, Defects as a root cause of fatigue failure of metallic components. II: non-metallic inclusions, Eng. Fail. Anal. 98 (2019) 228–239, doi:10.1016/j.engfailanal.2019.01.054.
[5] J. Monnot, B. Heritier, J. Cogne, J. Hoo, Relationship of melting practice, inclusion type, and size with fatigue resistance of bearing steels, Effect of Steel Manufacturing Processes on the Quality of Bearing Steels Ed., ASTM International, 1988 100 Barr Harbor Drive, PO Box C700, West Conshohocken, PA 19428-2959149-149–16, doi:10.1520/STP26232S.
[6] L. Holappa, O. Wijk, Inclusion engineering, Treatise On Process Metallurgy, Elsevier, 2014.
[7] R. Kiessling, N. Lange, Non-Metallic Inclusions in Steel, 2nd ed., The Metals Society, London, 1978.
[8] P. Lamagnere, D. Girodin, P. Meynaud, F. Vergne, A. Vincent, Study of elasto-plastic properties of microheterogeneities by means of nano-indentation measurements: application to bearing steels, Mater. Sci. Eng. A 215 (1996) 134–142, doi:10.1016/0921-5093(96)10268-9.
[9] A. Stiénon, A. Fazekas, J.Y. Buffière, A. Vincent, P. Daguier, F. Merchi, A new methodology based on X-ray micro-tomography to estimate stress concentrations around inclusions in high strength steels, Mater. Sci. Eng. A 513–514 (2009) 376–383, doi:10.1016/j.msea.2009.02.008.
[10] Y.N. Wang, J. Yang, Y.P. Bao, Effects of non-metallic inclusions on machinability of free-cutting steels investigated by nano-indentation measurements, Metall. Mater. Trans. A 46 (2015) 281–292, doi:10.1007/s11661-014-2596-3.
[11] C.F. Kusche, J.S.K.L. Gibson, M.A. Wollenweber, S. Korte-Kerzel, On the mechanical properties and deformation mechanisms of manganese sulphide inclusions, Mater. Des. 193 (2020) 108801, doi:10.1016/j.matdes.2020.108801.
[12] G. Žagar, V. Pejchal, M.G. Mueller, A. Rossoll, M. Cantoni, A. Mortensen, The local strength of microscopic alumina reinforcements, Acta Mater. 100 (2015) 215–223, doi:10.1016/j.actamat.2015.08.026.
[13] V. Pejchal, M. Fornabaio, G. Žagar, A. Mortensen, The local strength of individual alumina particles, J. Mech. Phys. Solids 109 (2017) 34–49, doi:10.1016/j.jmps.2017.08.005.
[14] M.G. Mueller, G. Žagar, A. Mortensen, *In-situ* strength of individual silicon particles within an aluminium casting alloy, Acta Mater. 143 (2018) 67–76, doi:10.1016/j.actamat.2017.09.058.
[15] J. Everaerts, A. Slagter, A. Mortensen, A method for cleaning flat punch diamond microprobe tips, Micron 155 (2022) 103217, doi:10.1016/j.micron.2022.103217.
[16] K.L. Johnson, Contact Mechanics, Cambridge university Press, 1987.
[17] C.R. Kurkjian, M.J. Matthewson, Mechanical strength and reliability of glass fibers, in: Specialty Optical Fibers Handbook, Elsevier, 2007, pp. 735–781, doi:10.1016/B978-012369406-5/50026-6.
[18] N.P. Bansal, R. Doremus, Handbook of Glass Properties, Academic Press, Orlando San Diego, 1986.
[19] G. Kermouche, E. Barthel, D. Vandembroucq, P. Dubujet, Mechanical modelling of indentation-induced densification in amorphous silica, Acta Mater. 56 (2008) 3222–3228, doi:10.1016/j.actamat.2008.03.010.
[20] S. Bruns, K.E. Johanns, H.U.R. Rehman, G.M. Pharr, K. Durst, Constitutive modeling of indentation cracking in fused silica, J. Am. Ceram. Soc. 100 (2017) 1928–1940, doi:10.1111/jace.14734.
[21] N. Aritomi, K. Gunji, Morphology and formation mechanism of dendritic inclusions in iron and iron-nickel alloys deoxidized with silicon and solidified unidirectionally, ISIJ Int. 19 (1979) 152–161, doi:10.2355/isijinternational1966.19.152.
[22] N. Aritomi, K. Gunji, On the formation of dendritic inclusion from a spherical primary silica in iron- lO% nickel alloy deoxidized with silicon, ISIJ Int. 20 (1980) 26–32, doi:10.2355/isijinternational1966.20.26.
[23] G. Forward, Nucleation of Oxide Inclusions During the Solidification of Iron, Massachusetts Institute of Technology MIT, 1966.
[24] A. Slagter, J. Everaerts, A. Mortensen, Nanoindentation of embedded particles, Under Review. (n.d.).
[25] D. Tuschel, Why are the Raman spectra of crystalline and amorphous solids different? Spectroscopy 32 (2017) 26–33 (Santa Monica).
[26] M.C. Flemings, B) Formation of oxide inclusions during solidification, Int. Met. Rev. 22 (1977) 201–207, doi:10.1179/imtr.1977.22.1.187.
[27] L. Zhang, B.G. Thomas, State of the art in the control of inclusions during steel ingot casting, Metall. Mater. Trans. B 37 (2006) 733–761, doi:10.1007/s11663-006-0057-0.
[28] J. Gleinig, A. Weidner, J. Fruhstorfer, C.G. Aneziris, O. Volkova, H. Biermann, Characterization of nonmetallic inclusions in 18CrNiMo7-6, Metall. Mater. Trans. B 50 (2019) 337–356, doi:10.1007/s11663-018-1431-4.
[29] K. Wasai, K. Mukai, Mechanism of formation of amorphous silica inclusion in silicon deoxidized copper, ISIJ Int. 43 (2003) 606–611, doi:10.2355/isijinternational.43.606.
[30] J.E. Shelby, Formation and properties of calcium aluminosilicate glasses, J. Am. Ceram. Soc. 68 (1985) 155–158, doi:10.1111/j.1151-2916.1985.tb09656.x.
[31] G. Kermouche, G. Guillonneau, J. Michler, J. Teisseire, E. Barthel, Perfectly plastic flow in silica glass, Acta Mater. 114 (2016) 146–153, doi:10.1016/j.actamat.2016.05.027.
[32] R. Ramachandramoorthy, J. Schwiedrzik, L. Petho, C. Guerra-Nuñez, D. Frey, J.M. Breguet, J. Michler, Dynamic plasticity and failure of microscale glass: rate-dependent ductile–brittle–ductile transition, Nano Lett. 19 (2019) 2350–2359, doi:10.1021/acs.nanolett.8b05024.
[33] Z. Tang, N.P. Lower, P.K. Gupta, C.R. Kurkjian, R.K. Brow, Using the two-point bend technique to determine failure stress of pristine glass fibers, J. Non Cryst. Solids 428 (2015) 98–104, doi:10.1016/j.jnoncrysol.2015.08.005.
[34] D. France, C.R. Kurkjian, Craig, the effect of environment on the strength of optical fiber, in: Strength of Inorganic Glass, Plenum Press, New York, 1985, pp. 309–328.
[35] C.R. Kurkjian, P.K. Gupta, R.K. Brow, The strength of silicate glasses: what do we know, what do we need to know? Int. J. Appl. Glass Sci. 1 (2010) 27–37, doi:10.1111/j.2041-1294.2010.00005.x.
[36] C.R. Kurkjian, O.S. Gebizlioglu, I. Camlibel, Strength Variations in Silica Fibers, in: Optical Fiber Reliability and Testing, Proc. SPIE, 3848, SPIE, Boston, MA, USA, 1999, pp. 77–86.
[37] M. Guerette, C.R. Kurkjian, S. Semjonov, L. Huang, Nonlinear elasticity of silica glass, J. Am. Ceram. Soc. 99 (2016) 841–848, doi:10.1111/jace.14043.
[38] P.K. Gupta, C.R. Kurkjian, Intrinsic failure and non-linear elastic behavior of glasses, J. Non Cryst. Solids 351 (2005) 2324–2328, doi:10.1016/j.jnoncrysol.2005.05.029.
[39] B.A. Proctor, I. Whitney, J.W. Johnson, The strength of fused silica, proceedings of the royal society of london. series A, Math. Phys. Sci. 297 (1967) 534–557.
[40] L.G. Baikova, T.I. Pesina, M.F. Kireenko, L.V. Tikhonova, C.R. Kurkjian, Strength of optical silica fibers measured in liquid nitrogen, Tech. Phys. 60 (2015) 869–872, doi:10.1134/S1063784215060031.
[41] C.R. Kurkjian, P.K. Gupta, R.K. Brow, N. Lower, The intrinsic strength and fatigue of oxide glasses, J. Non Cryst. Solids 316 (2003) 114–124, doi:10.1016/S0022-3093(02)01943-9.
[42] M.J. Matthewson, C.R. Kurkjian, S.T. Gulati, Strength measurement of optical fibers by bending, J. Am. Ceram. Soc. 69 (1986) 815–821, doi:10.1111/j.1151-2916.1986.tb07366.x.
[43] E. Suhir, Effect of the nonlinear stress-strain relationship on the maximum stress in silica fibers subjected to two-point bending, Appl. Opt. 32 (1993) 1567, doi:10.1364/AO.32.001567.
[44] E. Barthel, V. Keryvin, G. Rosales-Sosa, G. Kermouche, Indentation cracking in silicate glasses is directed by shear flow, not by densification, Acta Mater. 194 (2020) 473–481, doi:10.1016/j.actamat.2020.05.011.
[45] S. Bruns, T. Uesbeck, S. Fuhrmann, M. Tarragó Aymerich, L. Wondraczek, D. de Ligny, K. Durst, Indentation densification of fused silica assessed by raman spectroscopy and constitutive finite element analysis, J. Am. Ceram. Soc. 103 (2020) 3076–3088, doi:10.1111/jace.17024.
[46] D.M. Marsh, Plastic flow in glass, Proc. R. Soc. Lond. Ser. A Math. Phys. Sci. 279 (1964) 19, doi:10.1098/rspa.1964.0114.
[47] D. Wakabayashi, N. Funamori, T. Sato, Enhanced plasticity of silica glass at high pressure, Phys. Rev. B 91 (2015) 014106, doi:10.1103/PhysRevB.91.014106.
[48] R.N. Widmer, D. Bischof, J. Jurczyk, M. Michler, J. Schwiedrzik, J. Michler, Smooth or not: robust fused silica micro-components by femtosecond-laser-assisted etching, Mater. Des. 204 (2021) 109670, doi:10.1016/j.matdes.2021.109670.
[49] R. Lacroix, V. Chomienne, G. Kermouche, J. Teisseire, E. Barthel, S. Queste, Micropillar testing of amorphous silica, Int. J. Appl. Glass Sci. 3 (2012) 36–43, doi:10.1111/j.2041-1294.2011.00075.x.

[50] R. Lacroix, G. Kermouche, J. Teisseire, E. Barthel, Plastic deformation and residual stresses in amorphous silica pillars under uniaxial loading, Acta Mater. 60 (2012) 5555–5566, doi:10.1016/j.actamat.2012.07.016.
[51] G. Brambilla, D.N. Payne, The ultimate strength of glass silica nanowires, Nano Lett. 9 (2009) 831–835, doi:10.1021/nl803581r.
[52] B. E. Ramachandran, B. C. Pai, N. Balasubramanian, Studies on the acid resistance of E glass, J. Am. Ceram. Soc. (1980) Wiley Online Library, (n.d.), doi:10.1111/j.1151-2916.1980.tb10634.x.
[53] M.J. Matthewson, C.R. Kurkjian, J.R. Hamblin, Acid stripping of fused silica optical fibers without strength degradation, J. Lightwave Technol. 15 (1997) 490–497, doi:10.1109/50.557565.
[54] H.D. Chandler, R.L. Jones, Strength loss in ″E″ glass fibres treated in strong solutions of mineral acids, J. Mater. Sci. 19 (1984) 3849–3854, doi:10.1007/BF00980747.
[55] T. Geisler, A. Janssen, D. Scheiter, T. Stephan, J. Berndt, A. Putnis, Aqueous corrosion of borosilicate glass under acidic conditions: a new corrosion mechanism, J. Non Cryst. Solids 356 (2010) 1458–1465, doi:10.1016/j.jnoncrysol.2010.04.033.